

 **Very Important Publication**

Selective Aerobic Oxidation of 5-(Hydroxymethyl)furfural over Heterogeneous Silver-Gold Nanoparticle Catalysts

Oliver R. Schade,^{a, b} Frederic Stein,^{c, d} Sven Reichenberger,^{c, d} Abhijeet Gaur,^{a, b} Erisa Saraçi,^{a, b} Stephan Barcikowski,^{c, d} and Jan-Dierk Grunwaldt^{a, b, *}

^a Institute for Chemical Technology and Polymer Chemistry, Karlsruhe Institute of Technology (KIT), 76131 Karlsruhe, Germany
Phone: (+49) 721 608 42120

fax: (+49) 721 608 44820

E-mail: grunwaldt@kit.edu


^b Institute of Catalysis Research and Technology, Karlsruhe Institute of Technology (KIT), 76344 Eggenstein-Leopoldshafen, Germany


^c Technical Chemistry I, University of Duisburg-Essen, 45141 Essen, Germany

^d Center for Nanointegration Duisburg-Essen (CENIDE), University of Duisburg-Essen, 47057 Duisburg, Germany

Manuscript received: August 21, 2020; Revised manuscript received: September 21, 2020;

Version of record online: October 29, 2020

 Supporting information for this article is available on the WWW under <https://doi.org/10.1002/adsc.202001003>

 © 2020 The Authors. *Advanced Synthesis & Catalysis* published by Wiley-VCH GmbH. This is an open access article under the terms of the Creative Commons Attribution License, which permits use, distribution and reproduction in any medium, provided the original work is properly cited.

Abstract: Bimetallic silver-gold alloy nanoparticles on zirconia with varying Ag/Au ratios were designed by a rational approach and tested as catalysts for the selective oxidation of the promising biomass platform molecule 5-(hydroxymethyl)furfural (HMF). For this purpose, colloidal Ag_xAu_{10-x} particles with molar compositions $x=1/3/5/7/9$ were prepared by laser ablation in liquids, a surfactant-free method for the preparation of highly pure nanoparticles, before adsorption on zirconia. In-depth characterization of the supported catalysts evidenced alloyed nanoparticles with distinct trends of the surface and bulk composition depending on the overall Ag/Au molar ratio as determined by X-ray photoelectron spectroscopy (XPS) and X-ray absorption spectroscopy (XAS), respectively. To uncover the synergistic effect of the Ag/Au ratio, the catalysts were further studied in terms of the catalytic activity and selectivity in HMF oxidation. Either the aldehyde moiety or both functional groups of HMF were selectively oxidized depending on the Ag/Au composition resulting in 5-hydroxymethyl-2-furan-carboxylic acid (HFCA) or 2,5-furandicarboxylic acid (FDCA), respectively. Optimization of the reaction conditions allowed the quantitative production of HFCA over most catalysts, also after re-use. Only gold rich catalysts Ag₁Au₉/ZrO₂ and particularly Ag₃Au₇/ZrO₂ were highly active in FDCA synthesis. While Ag₃Au₇/ZrO₂ deactivated upon re-use due to sintering, no structural changes were observed for the other catalysts and all catalysts were stable against metal leaching. The present work thus provides fundamental insights into the synergistic effect of Ag and Au in alloyed nanoparticles as active and stable catalysts for the oxidation of HMF.

Keywords: bimetallic catalysts; FDCA; gold; heterogeneous catalysis; hydroxymethylfurfural; laser ablation; selective oxidation; silver; X-ray absorption spectroscopy

Introduction

The production of chemicals from renewable raw materials is becoming increasingly important as the growing demand for chemicals meets dwindling fossil

resources, which currently account for the largest share of raw materials in the chemical industry by far.^[1] One promising approach for the future synthesis of chemicals is the use of platform molecules from inedible biomass like lignocellulose.^[1b,2] Partial fragmentation

of biomass to sugars followed by acid-catalyzed dehydration results, for example, in 5-(hydroxymethyl) furfural (HMF), one of the most promising biomass platform molecules.^[2a,3] Among other reactions like hydrogenation,^[4] dehydrogenation^[5] or hydrodeoxygenation^[6] the selective oxidation of HMF has gained increasing interest in recent years,^[1c,7] particularly due to the structural similarity of 2,5-furandicarboxylic acid (FDCA) to terephthalic acid.^[1c,8] Because of its significance as a bio-derived monomer, FDCA was even listed as one of twelve important molecules that could be produced in an industrial scale by the U.S. Department of Energy.^[9] Selectively oxidizing the aldehyde moiety of HMF yields 5-hydroxymethyl-2-furancarboxylic acid (HFCA), which also has possible applications as a monomer^[1c,8] as well as a building block in high-value fine chemicals, like drugs.^[10]

The synthesis of FDCA starting from HMF has been studied using stoichiometric oxidants like KMnO_4 .^[11] As the production of stoichiometric waste should be circumvented,^[12] catalytic routes have been studied using homogeneous, heterogeneous, electro-, and biocatalysis.^[1c,7] Currently, the AMOCO process is used for the large-scale industrial synthesis of FDCA.^[13] FDCA is produced in 61% yield over a homogeneous Co/Mn/Br catalyst at 125 °C and 70 bar air in acetic acid as solvent.^[13a] Advantages such as simple separation of the catalyst have now shifted the focus more on the more demanding heterogeneously catalyzed oxidation. High FDCA yields are mostly obtained over noble metal catalysts like Ru, Pd, Pt or Au (Figure 1),^[1c,7,14] which often require the addition of a homogeneous base to enhance FDCA solubility and accelerate the reaction.^[15]

As it is mostly considered an intermediate in FDCA synthesis, a small number of studies focus on the targeted synthesis of HFCA. Besides a chemical synthesis using the Cannizzaro reaction,^[16] which is limited to a maximum HFCA yield of 50%, biocata-

lytic reactions were employed for HFCA synthesis.^[17] Also, heterogeneous catalysts gave high yields in organic solvents, which however affects the sustainability of the reaction.^[18] In contrast, supported Ag-based catalysts allow the quantitative production of HFCA in water under mild reaction conditions (Figure 1).^[19]

Bimetallic catalysts are of particular interest in HMF oxidation as they were reported to be more active and stable upon re-use.^[1c,7,20] The previously mentioned high selectivity of Ag towards HFCA and Au towards FDCA formation suggests that tuning the oxidation catalyst by alloy formation of Ag with Au appears to be especially attractive. However, to the best of our knowledge, this has not yet been conducted in HMF oxidation.

For other reactions it has been shown that bimetallic Ag–Au catalysts were more active in selective^[21] as well as total oxidation^[22] reactions, e.g. the superior activity of bimetallic Ag–Au catalysts in glucose oxidation was attributed to the activation of oxygen on Ag.^[21a] It is well known that oxygen activation is often challenging on Au-based oxidation catalysts,^[23] which on the other hand is favored on Ag. Hence, synergistic effects can be expected. In addition, both metals are fully miscible in every molar ratio.

To study how Ag modifies the Au catalyst for different molar ratios, catalysts with alloyed and comparable particle sizes are required. Despite their miscibility, the synthesis of alloyed Ag–Au nanoparticles is not straightforward. Preparation methods include sequential deposition-precipitation,^[24] co-impregnation,^[25] flame-spray pyrolysis,^[26] or colloidal preparation methods with chemical reduction.^[27]

The most commonly used precursors HAuCl_4 and AgNO_3 have several disadvantages, such as reduction of Au before Ag leading to the formation of a composition gradient throughout the bimetallic nanoparticle with a Au-rich core and a Ag-rich shell.^[28] Further, AgCl may precipitate parallel to the reduction and high chloride concentrations can lower the catalytic activity of Au-based catalysts.^[29] Working below the solubility limit of AgCl is impractical for the preparation of supported catalysts as these high dilutions complicate subsequent deposition.^[30] Finally, capping agents or ligands might also affect the catalytic activity by blocking the active sites.^[31] This may alter oxygen activation, catalytic activity, and selectivity in addition to the nanoparticle composition.

To overcome such shortcomings, a rational catalyst design is needed.^[32] Pulsed laser ablation in liquids (LAL) has shown to be a promising alternative for the preparation of metal, oxide, and alloy nanoparticle catalysts.^[33] In this method, a pulsed laser beam is focused onto the target immersed in a liquid, leading to rapid heating combined with the formation of a plasma plume. The superheated and evaporating material

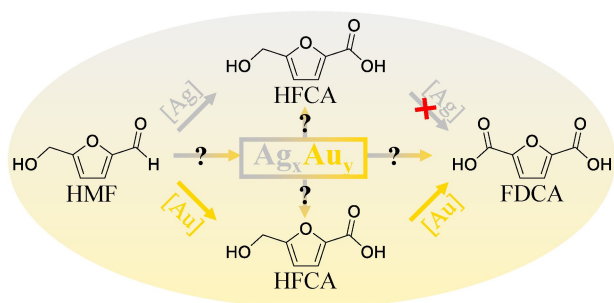


Figure 1. Schematic reaction mechanism of HMF oxidation in alkaline aqueous solution over gold- (bottom) and silver-based (top) catalysts. The activity, selectivity, and performance of bimetallic Ag–Au catalysts (middle) is the focus of this study.

subsequently forms a jet of superheated matter which gets injected into the overlying liquid phase on a timescale of 10 to 100 nanoseconds, inducing rapid cooling with up to 10^{12} K s^{-1} .^[34] Due to the heat transfer into the liquid, a cavitation bubble emerges, containing the nucleating and growing nanoparticles. The bubble collapses about 200 μs after the laser hits the target thereby releasing the nanoparticles.^[35] Because of the uniform and rapid evaporation and nucleation kinetics, LAL is an efficient method to generate surfactant-free Ag–Au nanoparticles with a homogeneous as well as average elemental distribution and high purity, rendering them as attractive systems to study the selectivity of Ag and Au for HMF oxidation to FDCA and HFCA.

Within this study, (1) $\text{Ag}_x\text{Au}_{10-x}/\text{ZrO}_2$ catalysts were prepared by supporting on ZrO_2 nanoparticles generated via LAL with systematically varying the molar composition (Ag/Au ratio $x = 1/3/5/7/9$) with comparable size and (2) applied in the selective oxidation of HMF to HFCA and FDCA. The overall strategy is shown in Figure 2a. After thorough catalyst characterization concerning structure and composition, the effect of alloy formation on the catalytic activity and selectivity in aldehyde and alcohol oxidation was explored. The catalytic reactions were carried out in an aqueous medium using air as the oxidant.

Results and Discussion

Rational Design and Characterization of the Catalysts

The general approach of this study is depicted in Figure 2a. Nanoparticles were synthesized by LAL with a monomodal size distribution with average hydrodynamic diameters of 6–7 nm, except for Ag_3Au_7 (12 nm) based on analytical disc centrifugation (ADC). The synthesis is described in detail in the experimental part and a scheme (Figure 2a) and photograph of the setup is given in the supporting information (Figure S1).

Respective particle size distributions are shown in Figure S3. From UV-Vis spectra of the resulting colloidal suspensions, shown in Figure 2b, single absorbance peaks that are shifted linearly with the composition of the particles can be observed (Figure 2c), indicating successful alloy formation.^[36] Although the optical properties of the nanoparticles also depend on their size and shape,^[37] the respective shifts are in line with literature where comparable particle sizes and shapes were investigated.^[38] Slight differences arise from the presence of stabilizing ligands during biological or chemical syntheses,^[39] whereas laser-generated alloy nanoparticles give the lowest surface plasmon resonance (SPR) wavelengths due to the absence of such agents.^[36a,40] Hence, LAL proves to be an ideal method for the synthesis of alloyed Ag–Au nanoparticles (AgAu NPs) compared to wet-chemical preparation.^[41] Successful electrostatic adsorption of the nanoparticles on ZrO_2 was achieved by colloidal deposition under careful pH adjustment as

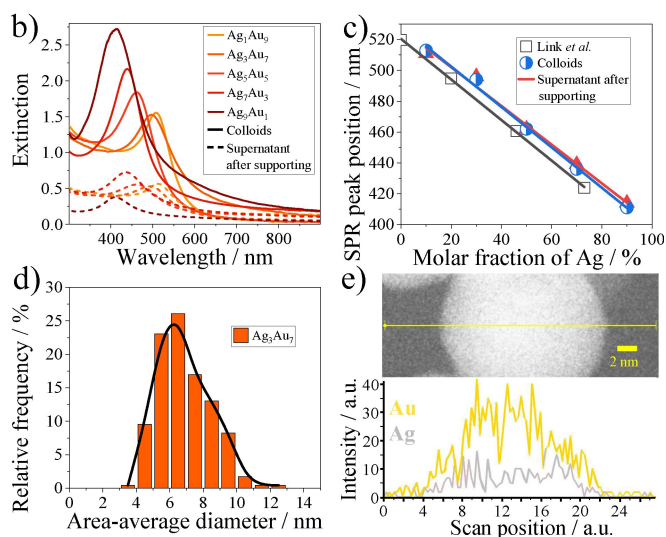
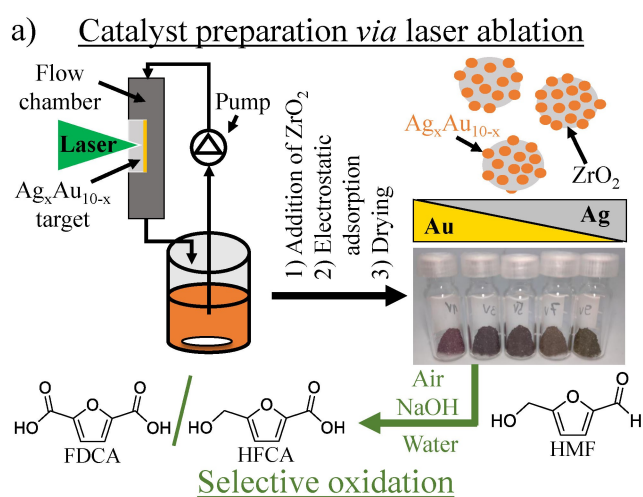


Figure 2. (a) Schematic approach of the study presented here and (b) UV-Vis spectra of the alloyed colloids before and after electrostatic adsorption on ZrO_2 , (c) linear shift of the SPR with increasing Au content and comparison to literature values from Link *et al.*,^[38] (d) representative particle size distribution of $\text{Ag}_3\text{Au}_7/\text{ZrO}_2$ based on TEM and (e) representative EDX line scan of Ag_3Au_7 particles.

Table 1. Metal loading and specific surface area of the supported catalysts and the ZrO₂ support material.

Entry	Catalyst/Support	Metal loading/wt. %	Specific surface area/m ² g ⁻¹	Mean particle size/nm ^[a]	Ag:Au molar ratio ^[b]
1	-/ZrO ₂	-	99	-	
2	Ag ₁ Au ₉ /ZrO ₂	1.5	99	9.4 ± 1.4	11:89 (10:90)
3	Ag ₃ Au ₇ /ZrO ₂	1.3	98	6.9 ± 1.6	32:68 (30:70)
4	Ag ₅ Au ₅ /ZrO ₂	1.3	100	8.1 ± 2.2	53:47 (50:50)
5	Ag ₇ Au ₃ /ZrO ₂	0.7	100	9.9 ± 2.1	74:26 (70:30)
6	Ag ₉ Au ₁ /ZrO ₂	1.4	98	11.4 ± 1.9	90:10 (90:10)

^[a] Mean particle size based on TEM.

^[b] Values from ICP-OES with theoretical values given in brackets for comparison.

previously described^[42] and was observed both by the significant color change of the initially white ZrO₂ powder (Figure 2a) and the depletion of AgAu NPs in the colloidal suspensions (Figure 2b) during the deposition process. After removing the aqueous supernatant, Ag_xAu_{10-x}/ZrO₂ catalysts were dried and characterized by DR-UV-Vis confirming the successful adsorption of AgAu NPs on the support (Figure S4a). In accordance with UV-Vis measured of the initial colloids, a composition-dependent linear shift of the SPR peak was found (Figure S4b). The presence of the nanoparticles on the ZrO₂ support was further evidenced by STEM analysis. Particle size distributions, exemplarily shown for Ag₃Au₇/ZrO₂ in Figure 2d (for all other catalysts cf. Figures S14–S15), and mean particle sizes were derived from STEM images of the supported catalysts (Table 1). From the comparison to the initial size distributions measured for the colloids by ADC, the nanoparticle size of colloidal AgAu NPs were maintained after the deposition process for all catalysts (see Figure S15). In accordance with ADC measurements conducted before colloidal deposition, AgAu NP sizes of 7–11 nm were also found by STEM on the ZrO₂ support after deposition. Consequently, particle sizes were maintained during the deposition reported previously in other studies for laser-generated catalysts.^[33b,43] EDX line scans of representative Ag₁Au₉/ZrO₂ and Ag₃Au₇/ZrO₂ catalysts showed a homogeneous distribution of both metals along the particle diameters (Figure 2e, Figures S16–S17). ICP-OES verified the metal loading to be close to 1.5 wt. % in all but one case (Table 1). Additionally, the Ag/Au molar ratios are well in line with the nominal compositions of the target alloys. It can be observed from N₂ physisorption, that the specific surface area was maintained during the colloidal AgAu NP deposition process (Table 1). Since the deviations are within the margin of error, we can conclude that the support was not changed during the adsorption process and no pores were blocked by the metal particles, further confirmed by similar pore sizes of the pure ZrO₂ and the supported catalysts.

All catalysts were examined *via* XAS to further unravel the local electronic structure (oxidation state),

charge transfer phenomena, and alloy formation. The former two can be derived from the X-ray absorption near edge structure (XANES) while the extended X-ray absorption fine structure (EXAFS) provides information about alloy formation, as it is sensitive to the different backscattering of Ag and Au neighbors.^[44] The overall oxidation state of Au can be estimated from the XANES region by the area of white line features in the Au L₃ spectra, which is related to the density of d states of the absorbing Au atom.^[45] This area can be correlated to the d-electronic structure by using the difference spectrum obtained from the Au L₃- and the L₂-edge XANES spectra, which gives a single distinct peak.^[44a,45–46] Figure 3a shows the normalized Au L₃ XANES spectra of the catalysts along with Au foil for comparison. From the XANES features, Au is in the metallic state in all catalysts.

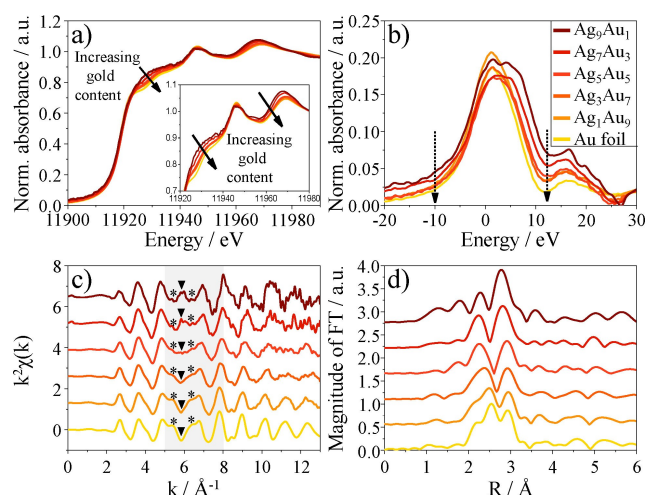


Figure 3. Proof of alloy formation and insights into the Au oxidation state using XAS. (a) Au L₃ XANES spectra, (b) difference curves obtained by subtracting the Au L₂-edge metal foil spectrum from the Au L₃-edge spectra of samples and Au foil, (c) k² weighted $\chi(k)$ spectra and (d) Fourier transformation of the k²-weighted EXAFS spectra of the different Ag_xAu_{10-x}/ZrO₂ (x = 1/3/5/7/9) catalysts. Changes observed in $\chi(k)$ spectra (c) due to alloy formation are highlighted by corresponding symbols and the grey area.

However, the spectra differ in the white line region (11920–11940 eV) and in the post-edge region (11960–11980 eV) as shown in the inset of Figure 3a. The variation in the white line feature can be attributed to electron transfer between Au and Ag. Figure 3b shows the corresponding difference spectra obtained by subtracting the Au L₂-edge spectrum of Au foil from the samples where a single peak with varying width and area is obtained (Table 2, detailed procedure in Supporting Information and Figure S2). In general, the calculated areas for AgAu catalysts are larger as compared to pure Au foil, thereby indicating Ag–Au interaction, i.e. due to alloy formation. The larger area of Ag₁Au₉, compared to Au foil (Table 2, entries 1–2) indicates an increase in the d-hole density.^[45] Hence, even at a low Ag fraction an electron transfer between Au and Ag is evident confirming strong Ag–Au interaction, e.g. by alloy formation. From Ag₁Au₉ to Ag₅Au₅ (Table 2, entries 2–4), the areas decrease with increasing Ag content. This reflects a decreasing number of d-holes, but all areas remain larger as compared to pure Au foil, thereby indicating Ag–Au interaction. Based on the variation in the d-hole density, the interaction between Au and Ag appears to vary with the molar ratios. From this trend, more Ag atoms appear present in the outer layer while higher Au atom concentration is located in the center for Ag-rich composition. On the other hand, a high Ag fraction in Ag₇Au₃ and Ag₉Au₁ seems to lead to diffusion of Ag atoms into the center as evidenced by the increase in the corresponding areas (Table 2,

entries 5–6). The k²-weighted $\chi(k)$ EXAFS spectra for the Ag_xAu_{10-x} catalysts are shown in Figure 3c in comparison to Au foil and corresponding Fourier transformed (FT) spectra are given in Figure 3d (fits given in Figures S12–S13). EXAFS oscillations in the k-region from 5–8 Å⁻¹ change with increasing Ag content, which correspond to the increase of Ag neighbors around the absorbing Au atom with different backscattering phase shifts at higher k.^[47] In the FT spectra, the metal-metal scattering doublet peaks shift towards lower R with increasing Ag content, which also points towards replacement of Au atoms by Ag atoms i.e. an increase in Au–Ag coordination. The first shell contribution which appears as a double peak can be attributed to the interference between Au–Au and Au–Ag backscattering with different phase shift and amplitude. EXAFS analysis was performed to derive the degree of alloying by comparing the fitted coordination number (CN) with the composition (Table 3).

For Ag₁Au₉, the CN_{Au–Au} of 12.1 (Au–Au 2.85 Å) is close to its value in Au foil and no Au–Ag scattering was observed. On the other hand, a lower CN_{Au–Au} of 10.5 was found for Ag₃Au₇. Here Au–Ag scattering occurred with a CN_{Au–Ag} of 2.2 at 2.86 Å. For a homogeneously mixed alloy, the ratio of CN_{Au–Au} to CN_{Au–Ag} should be close to the molar ratio of Au:Ag.^[48]

Since XAS is a volume-sensitive method, spatially resolved information e.g. on the composition of the surface can only be derived indirectly from comparison of the ratio of Au–Au and Au–Ag CNs as well as their deviation from the expected values for homogeneous composition. The ratio of CNs is shown in the last column of Table 3. Evidently, the ratio of CNs is higher in gold while ICP verified that the overall composition agrees well with the nominal composition (Table 1). Hence, a small composition gradient with Ag slightly enriched in the surface-near volume is expected for some compositions.^[49] For Ag₇Au₃, the ratio of CNs is closest to the molar ratio (Table 3,

Table 2. Area under the marked region in Figure 3b.

Entry	Sample	$\Delta A3/\text{eV cm}^{-1}$
1	Au foil	1.67 ± 0.03
2	Ag ₁ Au ₉	1.92 ± 0.02
3	Ag ₃ Au ₇	1.80 ± 0.03
4	Ag ₅ Au ₅	1.75 ± 0.03
5	Ag ₇ Au ₃	1.89 ± 0.05
6	Ag ₉ Au ₁	2.44 ± 0.11

Table 3. EXAFS fitting results obtained from Au L₃-edge absorption spectra of Ag_xAu_{10-x}/ZrO₂; EXAFS spectra were fitted in the range of R = 1.0–3.4 Å and k = 2.4–12.7 Å⁻¹ using k_w = 2.

Entry	Sample	CN _{Au–Au}	R/Å	$\sigma^2 \cdot 10^{-3}/\text{Å}^2$	CN _{Au–Ag}	R/Å	$\sigma^2 \cdot 10^{-3}/\text{Å}^2$	$\Delta E0/\text{eV}$	CN _{Total}	Ag: Au ratio ^[a, b]
1	Au foil	12.0 ^[c]	2.86 ± 0.02	7.7 ± 0.4	–	–	–	4.8 ± 0.5	12.0	–
2	Ag ₁ Au ₉	12.1 ± 0.8	2.85 ± 0.03	9.2 ± 0.5	–	–	–	4.6 ± 0.5	12.1	– (10:90)
3	Ag ₃ Au ₇	10.5 ± 1.4	2.85 ± 0.03	9.9 ± 1.5	2.2 ± 0.8	2.86 ± 0.10	7.9 ± 2.8	4.6 ± 0.8	12.7	17:83 (30:70)
4	Ag ₅ Au ₅	7.1 ± 1.7	2.85 ± 0.03	7.5 ± 2.0	3.9 ± 1.2	2.84 ± 0.07	7.9 ± 2.4	4.2 ± 1.2	11.0	35:65 (50:50)
5	Ag ₇ Au ₃	3.9 ± 1.6	2.85 ± 0.04	5.4 ± 2.8	6.7 ± 1.4	2.84 ± 0.08	7.8 ± 1.7	4.3 ± 1.2	10.6	63:37 (70:30)
6	Ag ₉ Au ₁	–	–	–	10.1 ± 2.6	2.88 ± 0.12	9.7 ± 2.0	4.8 ± 1.7	10.1	– (90:10)

^[a] based on CNs from EXAFS fitting.

^[b] theoretical values are given in brackets.

^[c] fixed during the fitting.

entry 5). Hence, a homogeneous alloy is more probable in this case.

For Ag_9Au_1 , no Au–Au scattering was observed, but a Au–Ag CN of 10.1 was found. Since the total CNs for Ag_7Au_3 and Ag_9Au_1 are less than its maximum value of 12, this indicates the presence of an increased Au atom fraction on the surface. In summary, apart from the successful alloy formation, slight compositional gradients of the alloy nanoparticles are indicated by the EXAFS and XANES analysis.

To further investigate the oxidation state and the surface-near alloy composition, a complementary XPS study has been conducted with the as-prepared $\text{Ag}_x\text{Au}_{10-x}/\text{ZrO}_2$ catalysts and the results are given in Figure 4. The molar fraction of Au in the outer surface layers of $\text{Ag}_x\text{Au}_{10-x}/\text{ZrO}_2$ catalysts gained from XPS is given in Figure 4a, where the as-prepared, gold-rich $\text{Ag}_1\text{Au}_9/\text{ZrO}_2$ and $\text{Ag}_3\text{Au}_7/\text{ZrO}_2$ catalysts in Figure 4a show an enrichment of the surface with Ag. This is in line with EXAFS analysis. On the other hand, the surface composition is closest to the nominal composition for Ag_5Au_5 . At higher Ag content, more Au appears to be present on the surface of the catalysts before the reaction. Note upfront that after the catalytic reaction, the compositional gradient disappeared for low gold contents (shift toward nominal composition), while it was still present after reaction at gold molar fractions above 50%. From XPS peak deconvolution summarized in Figures S6–S9, the surface oxidation of the Au 4f and Ag 3d peaks has been extracted and summarized in Figure 4b. Therein, a correlation of the amount of oxidized atomic species of gold and silver is evident, respectively. In this context, XRD patterns of the bulk catalyst showed that the (111) reflections of Ag and Au at 38.2° decreased with higher Ag content (Figure S10). Taking the large extent of oxidized Ag surface atoms found by XPS into account, the decrease

of the (111) reflection with increasing Ag content appears to indicate the presence of small Au crystallites and amorphous oxidized Ag phases on the surface. On the other hand, for gold-rich compositions a higher crystallinity is evident in XRD, which is in line with the slight silver enrichment in the surface near volume observed in XPS for Ag_3Au_7 and Ag_1Au_9 (compare Figure 4a). Additionally, for gold-rich compositions, less oxidized gold atoms are present in the outer nanoparticle region while the percentage of oxidized silver atoms rises to a limited extent. In turn, a high silver content leads to a higher content of gold atoms present in oxidized form, such as silver renders gold to become less noble as previously discussed in the literature.^[50] Consequently, an electronic interaction of Au and Ag atoms is evident and in line with the results from XANES. In summary, by combining different X-ray based, optical and element-specific techniques, a successful alloy nanoparticle preparation of the desired composition has been proven. Slight element-enrichment at the nanoparticle surface has been observed with about 10% more Ag present at the surface in case of high Au content or about 10% enrichment of Au at the surface, in case of high Ag content. Compared to wet-chemical nanoparticles, which always show strong enrichment of Ag in the surface-near volume due to preferential reduction of more noble Au-based precursors, the laser-generated catalysts show a gradual elemental composition of the surface-near volume. In addition, they hit the right size regime reported to be active for Au-based catalysts for HMF to FDCA oxidation.^[51] Consequently, these laser-generated catalysts are ideal candidates for studying the influence of the Ag content on the catalytic activity and selectivity, presented in the following section.

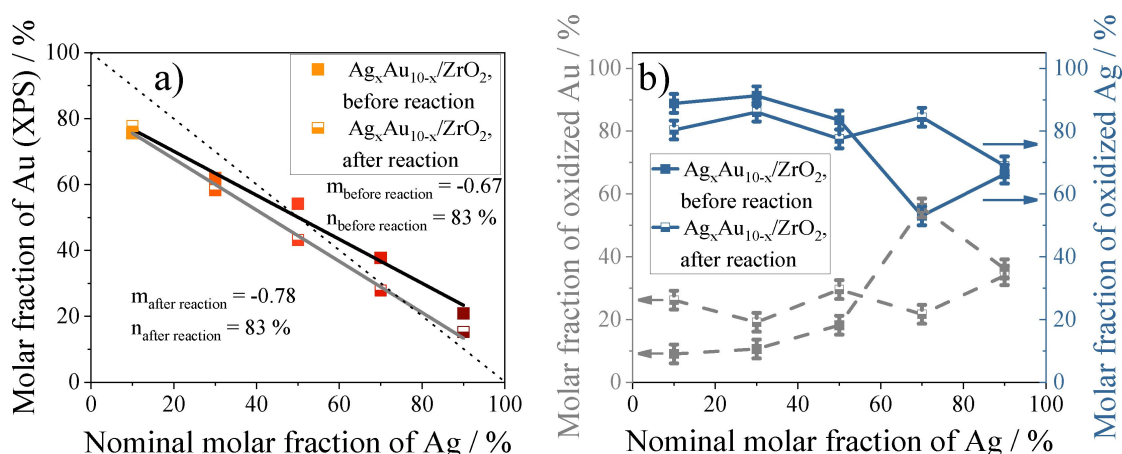


Figure 4. (a) Molar fraction of Au in the outer surface layers of AgAu/ZrO_2 catalysts gained from XPS. Molar fraction is balanced with the sum of Au and Ag; (b) Molar fraction of oxidized Au and Ag gained from XPS (cf. Figures S6–S9), shown for the as-prepared catalyst before reaction as well as the same catalysts after reaction.

Selective Oxidation of HMF by the Supported $\text{Ag}_x\text{Au}_{10-x}$ Particles

After thorough characterization, the catalysts were tested in the selective oxidation of HMF. First, the oxidation reactions were performed at different temperatures to investigate its influence on the activity and selectivity. The reactions were performed in the presence of 4 equivalents of NaOH, 10 bar air pressure and a constant HMF-to-metal molar ratio (HMF:M; M = sum of Ag and Au content) of 100:1 (Figure 5).

All catalysts were found to be active in the selective oxidation of HMF even at room temperature, where HFCA was produced as the main product. The highest HFCA yield of 95% under these conditions was achieved over $\text{Ag}_1\text{Au}_9/\text{ZrO}_2$. Increasing the reaction temperature caused the HFCA yield to pass through a maximum for Ag_3Au_7 , Ag_5Au_5 , and Ag_7Au_3 at 50 °C, 75 °C, and 75 °C, respectively, where HFCA was quantitatively produced over $\text{Ag}_5\text{Au}_5/\text{ZrO}_2$. Increasing the reaction temperature led to decreasing HFCA yields for all catalysts. Yet, FDCA production started at 100 °C over Ag_1Au_9 , Ag_3Au_7 , and Ag_5Au_5 , reaching up to 31%, 74%, and 29% yield at 125 °C, respectively. Carbon balances of less than 100% in some reactions can be attributed to the formation of unquantified so-called humins by multiple side-reactions of HMF in alkaline solution.^[52]

The formation of HFCA as the primary oxidation product at room temperature confirms that the oxidation of the aldehyde moiety of HMF proceeds readily and that the oxidation of the hydroxymethyl group is the rate-limiting step in alkaline conditions.^[53] The fact that the reaction temperature barely affected the activity and HFCA yield of the Ag_9Au_1 catalyst up to 100 °C can be attributed to the high Ag content (Table 1, entry 6), in line with literature on pure silver-based catalysts.^[19]

The oxidation of the hydroxymethyl group to finally form FDCA proceeded both at higher temperatures and increasing Au content, probably because Ag is inactive in this reaction.^[19a] Surprisingly, Ag_1Au_9

with the highest Au content gave a lower FDCA yield of 31% at 125 °C compared to Ag_3Au_7 (74%), while Ag_5Au_5 gave a similar yield of 29%. The optimum of FDCA production over Ag_3Au_7 , may be attributed to two effects: particle size or alloy composition. In general, the particle size is an important factor in pure Au catalysis, although Au catalysts in the given size range ($\approx 7\text{--}11$ nm, Table 1) were all found active in FDCA production.^[51,54] Note, that for CO oxidation, a reduced effect of particle size was found for alloy formation with Ag.^[55] Thus, the particle composition seems to have a stronger effect on FDCA production, with an optimal Ag/Au composition for both aldehyde and alcohol oxidation. Generally, the catalytic tests uncovered a pronounced effect of the catalyst composition on the product distribution at different temperatures.

Next, the influence of added NaOH on the product distributions was studied (Figure 6). Temperatures that gave the maximum production of HFCA were chosen for all catalysts except Ag_3Au_7 , which was highly active in FDCA production at 125 °C. The respective temperatures are indicated for each composition in Figure 6. Lowering the amount of added base is relevant both ecologically and economically, as increasing the pH of a HMF solution prior to acidic separation of FDCA leads to the production of large quantities of salt.^[12]

As can be seen in Figure 6 (discussed from right to left), decreasing the amount of added NaOH by half had no effect on the production of HFCA over Ag_1Au_9 , Ag_5Au_5 , Ag_7Au_3 , and Ag_9Au_1 , all of which gave a constant HFCA yield. Further decreasing the added NaOH to one equivalent regarding HMF led to a slightly lower yield of HFCA; however, it had no effect for silver-rich alloys such as Ag_7Au_3 and Ag_9Au_1 , which both produce HFCA with a relatively constant yield of 80–85%. Hence, these catalysts are active also under conditions which are less alkaline and more environmentally favorable.

In the absence of NaOH, negligible or low HMF conversion and HFCA formation was observed. The

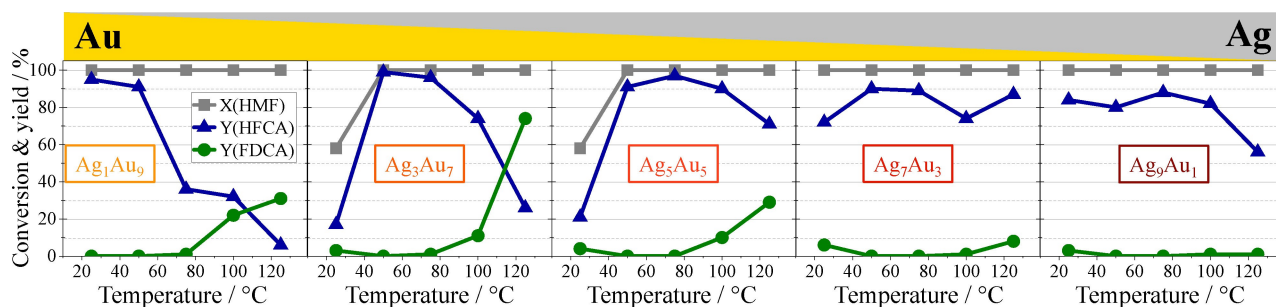


Figure 5. Variation of the reaction temperature using the different $\text{Ag}_x\text{Au}_{10-x}/\text{ZrO}_2$ catalysts. Reaction conditions: 10 bar air, HMF:NaOH 1:4, HMF:M 100:1, 5 h reaction time, 1 mmol HMF in a total volume of 10 mL.

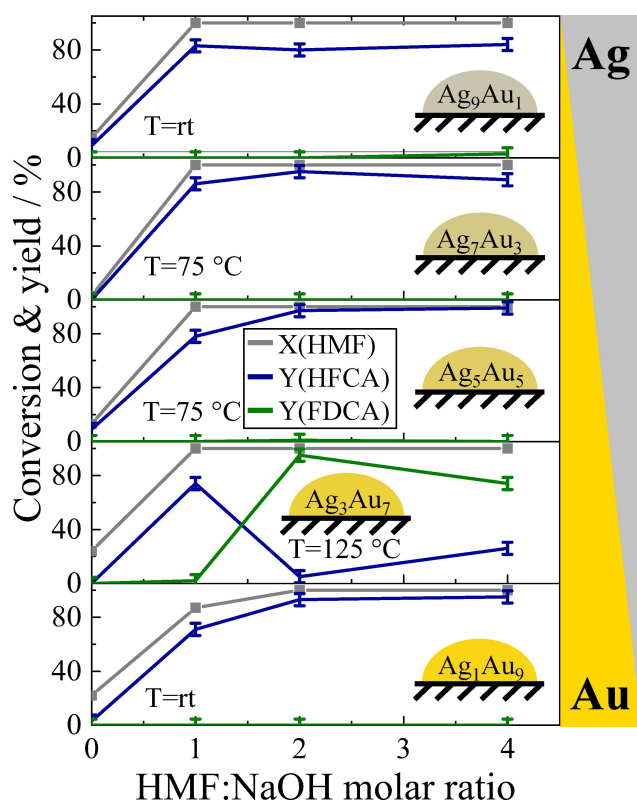


Figure 6. Variation of the added base using the different $\text{Ag}_x\text{Au}_{10-x}/\text{ZrO}_2$ catalysts at different temperatures that were previously optimized (Figure 5). Reaction conditions: 10 bar air, HMF:NaOH:M 1:0/1/2/4:100, 5 h reaction time, 1 mmol HMF in a total volume of 10 mL.

lowest HMF conversion of 3% was observed for Ag_7Au_3 , where no oxidation products were detected. On the other hand, for gold-rich catalysts $\approx 20\text{--}25\%$ of HMF was converted, while the yield of HFCA and FDCA was below 5% (selectivity below 15%). A maximum HFCA yield of 9% was gained from Ag_5Au_5 and Ag_9Au_1 catalysts at 13% and 15% HMF conversion, representing high selectivities of 68% and 62%, respectively.

As for Ag_3Au_7 , for which a temperature of 125°C was chosen for FDCA production, reduction of the added NaOH to two equivalents even resulted in an increase of FDCA yield to 95%. At one equivalent of added NaOH, HFCA was produced as the main product in 74% yield (2% FDCA yield). Under base-free conditions, HMF conversion dropped to 24% while no oxidation products were formed.

These results show that for the present catalysts one equivalent of hydroxide is required to achieve high HMF conversion and HFCA yield. In addition, FDCA production was observed over Ag_3Au_7 only when two or more equivalents of hydroxide were present. Hence, the reaction mechanism seems to involve a nucleophilic attack of a hydroxide ion on the aldehyde moiety

of HMF with subsequent dehydrogenation of the formed geminal diol.^[15,56] Another role of the homogeneous base may be to prevent catalyst deactivation by precipitation of poorly soluble FDCA onto the catalyst.

To compare the performances of all catalysts with literature (see Table S2), the productivity, i. e. moles of product formed normalized to the noble metal content and reaction time, was calculated. The highest productivity for HFCA of $19 \text{ mol}_{\text{HFCA}} \text{ h}^{-1} \text{ mol}_{\text{metal}}^{-1}$ was obtained over Ag_5Au_5 in the presence of two equivalents of NaOH. A similar FDCA productivity of $19 \text{ mol}_{\text{FDCA}} \text{ h}^{-1} \text{ mol}_{\text{metal}}^{-1}$ was observed over Ag_3Au_7 in the presence of two equivalents of NaOH.

In general, the variation in the amount of the added base revealed that the catalysts are active even in the presence of less base. Also, some activity was observed in the base-free oxidation of HMF over some catalysts; however, longer reaction times may aid to achieve higher yields of HFCA. Alternatively, solid bases could be used as support materials in future studies as reported recently.^[57]

In a next set of reactions, the influence of oxygen partial pressure was studied. An air pressure of 10 bar was chosen in the previous experiments. Oxygen participates indirectly in the reaction mechanism by removing hydrogen adsorbed on the catalyst surface.^[15,56] The hydrogen is formed during the dehydrogenation of the intermediately formed geminal diol from nucleophilic addition of hydroxide ions to the aldehyde group.^[15] Thus, despite gas phase oxygen not being directly incorporated into the oxidation product, its presence is crucial. Using air enhances the sustainability of the reaction,^[12] but the low concentration of oxygen makes its use more challenging compared to pure oxygen. To further elucidate the role of oxygen, reactions were performed at ambient pressure under previously optimized conditions (Table 4).

In general, the lower air pressure resulted in lower product yields over all catalysts except of Ag_9Au_1 , which gave a constant HFCA yield of 80% (Table 4, entry 5). The HFCA yield over Ag_1Au_9 (Table 4, entry 1) decreased from 95% at 10 bar ($19 \text{ mol}_{\text{HFCA}} \text{ h}^{-1} \text{ mol}_{\text{metal}}^{-1}$) to 77% at 1 bar air ($15 \text{ mol}_{\text{HFCA}} \text{ h}^{-1} \text{ mol}_{\text{metal}}^{-1}$). HFCA yields over Ag_5Au_5 and Ag_7Au_3 decreased more strongly to 25% and 18%, respectively. Also, the FDCA yield over Ag_3Au_7 dropped from 98% ($19 \text{ mol}_{\text{FDCA}} \text{ h}^{-1} \text{ mol}_{\text{metal}}^{-1}$, 2% HFCA yield) at 10 bar to just 3% ($1 \text{ mol}_{\text{FDCA}} \text{ h}^{-1} \text{ mol}_{\text{metal}}^{-1}$, 17% HFCA yield) at ambient pressure (Table 4, entry 2).

These results underline differences in activity and selectivity depending on the composition of Ag–Au catalysts and demonstrate the crucial role of oxygen in the selective oxidation of HMF. Depending on the Ag/Au ratio, the effect of oxygen partial pressure differed. Previous studies on HFCA synthesis over

Table 4. Variation of the applied air pressure using the different $\text{Ag}_x\text{Au}_{10-x}/\text{ZrO}_2$ ($x = 1/3/5/7/9$) catalysts at different temperatures and amounts of added NaOH that were previously optimized. Reaction conditions: HMF:M 100:1, 5 h reaction time, 1 mmol HMF in a total volume of 10 mL.

Entry	Catalyst	Pressure			10 bar		
		1 bar X(HMF)	Y(HFCA)	Y(FDCA)	X(HMF)	Y(HFCA)	Y(FDCA)
1	Ag_1Au_9 ^[a,c]	100	77	0	100	95	0
2	Ag_3Au_7 ^[a,d]	100	17	3	100	5	95
3	Ag_5Au_5 ^[a,e]	100	25	3	100	97	1
4	Ag_7Au_3 ^[a,e]	100	18	2	100	95	0
5	Ag_9Au_1 ^[b,c]	100	80	0	100	83	0

Individual reaction conditions:

[a] two equivalents of NaOH.

[b] one equivalent of NaOH.

[c] room temperature.

[d] 125 °C.

[e] 75 °C.

pure Ag catalysts revealed a minor influence of air pressure,^[19a] which also seems to be the case for bimetallic Ag–Au catalysts rich in Ag like Ag_9Au_1 . That might be attributed to favored adsorption of oxygen on Ag as compared to Au with the reaction proceeding on neighboring Au active sites.^[21a] This is further confirmed by comparison of the Ag-rich Ag_9Au_1 to Au-rich Ag_1Au_9 , both of which were tested at room temperature. The more pronounced decrease in HFCA yield over silver-depleted Ag_1Au_9 confirms that Au-based or in this case Au-rich catalysts are more influenced by air pressure due to limited oxygen adsorption. Hence, catalysts rich in gold generally require higher air pressure to achieve high product yields.

Neither Au nor Ag were found in the reaction solutions of all catalysts by ICP-OES, showing that the catalysts are stable against metal leaching in solution.

The productivity of Ag_3Au_7 towards FDCA of $19 \text{ mol}_{\text{FDCA}} \text{ h}^{-1} \text{ mol}_{\text{metal}}^{-1}$ is in the range or higher as compared to other alloys like AuPd ^[20a,58] or AuCu ^[59] in literature (Table S2), which underlines the potential of Ag–Au alloys as highly active catalysts for HMF oxidation. However, note that comparability should be taken with caution due to different reaction conditions like the addition of a base.

In a final step after optimizing reaction temperature, added NaOH and air pressure, the temporal progression of the reactions was studied (Figure 7). For Ag_1Au_9 and Ag_9Au_1 , which were tested at room temperature, a classical batch process conversion profile starting from no HMF conversion at $t=0$ was observed. HMF was very rapidly and selectively converted to HFCA over Ag_1Au_9 , which gave HFCA in 64% yield (76% selectivity) after 30 min. Quantitative HMF conversion was observed after 1 h giving 83% HFCA yield at $83 \text{ mol}_{\text{HFCA}} \text{ h}^{-1} \text{ mol}_{\text{metal}}^{-1}$ productiv-

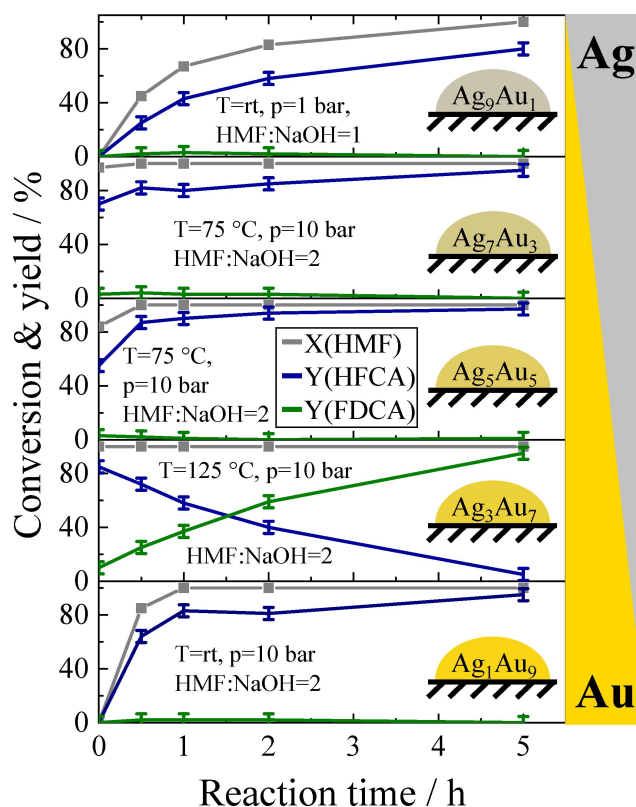


Figure 7. Temporal evolution of HMF oxidation using the different $\text{Ag}_x\text{Au}_{10-x}/\text{ZrO}_2$ catalysts under different reaction conditions that were previously optimized. Reaction conditions: 1 mmol HMF in a total volume of 10 mL, HMF:M 100:1.

ity. Prolonged reaction time led to an increase in HFCA yield up to 95% after 5 h, despite the quantitative conversion of HMF after just 1 h, which might be attributed to adsorbed intermediates or the product itself on the catalyst surface. On the other

hand, HMF conversion and HFCA yield steadily increased with time over Ag_9Au_1 , which can be attributed to the milder reaction conditions. However, longer reaction times are required to achieve high HMF conversion and HFCA yield under ambient conditions.

In case of the intermediate compositions Ag_3Au_7 , Ag_5Au_5 , and Ag_7Au_3 , conversions of HMF in Figure 7 were found to be high already at $t=0$. This observation is linked to the definition of the starting time $t=0$, which was set to reaching the desired reaction temperature for the first time. For example, reaching 125°C for Ag_3Au_7 took about 15 min. Consequently, for Ag_3Au_7 , high product yields of 85% HFCA and 10% FDCA were already achieved at the nominal start of the reaction. This shows Ag_3Au_7 is extremely active in aldehyde oxidation, which is already quantitatively converted during heating up. With longer reaction times, HFCA yield decreased linearly with a linear increase in FDCA yield, pointing out alcohol oxidation as the rate-limiting step.^[53] Therefore, a reaction time of 5 h is required to produce FDCA in 95% yield. The fact that no 5-formyl-2-furancarboxylic acid (FFCA) is found, which is the intermediate of HFCA oxidation to FDCA,^[15] underlines the high activity in aldehyde oxidation. Note that for all catalysts not tested under ambient conditions, the aldehyde oxidation activity is even higher, since high yields are obtained despite harsher reaction conditions in terms of HMF stability.

The influence of the HMF:M ratio was studied by decreasing the amount of catalyst added to the reaction solution, (Figure S19) resulting in increased productivity rates up to $254 \text{ mol}_{\text{HFCA}} \text{ h}^{-1} \text{ mol}_{\text{metal}}^{-1}$ for Ag_5Au_5 at a HMF:M ratio of 300. Decreasing HMF conversion or product yields upon the addition of less catalyst showed that the reactions performed so far were not limited by solid-liquid mass transfer. If reactions are scaled up at a later stage, however, mass transfer limitations have to be considered. To study possible mass transfer effects, the oxidation of HMF over $\text{Ag}_9\text{Au}_1/\text{ZrO}_2$ was scaled up to 30 mL by a factor of three. As in the previous reactions, the catalyst was used as a fine powder to minimize possible internal mass transport limitations. With increasing reaction volume, good mixing becomes increasingly important to maintain a slurry, which minimizes solid-liquid transfer limitations. To study the effect of mixing at the increased volume of 30 mL, the stirring speed was varied by almost an order of magnitude, (150–1400 rpm, Figure S20) and the HFCA yield was increased accordingly (5–30%), revealing that the reaction was limited to some extent by solid-liquid mass transfer in the bigger reaction volume. Next, the reaction was performed in a special reactor equipped with a mechanical gas entrainment impeller for better mixing of the liquid phase and enhancement of the gas-liquid interface, thus better gas-liquid mass trans-

fer. It was found that a high HFCA yield of 82% could be reached within 2 h ($41 \text{ mol}_{\text{HFCA}} \text{ h}^{-1} \text{ mol}_{\text{metal}}^{-1}$) with optimal mixing of the different phases of the reaction. The profiles are similar but with a higher productivity, evidencing that with careful considerations, a future scale-up is indeed possible.

Catalyst Stability and Reuse

Catalysts were separated from the reaction mixture and dried overnight before testing in a subsequent reaction under identical conditions for reusability studies (Figure 8 a–e). A slight loss of catalyst mass during this recycling process was taken into account by adjusting the amount of reactant and total volume to the recovered catalyst mass. Ag_1Au_9 , Ag_5Au_5 , and Ag_7Au_3 proved very stable upon reuse, and the product yield and productivity rate remained constant for five reuse cycles. Particle sizes did not severely change for these catalysts (Figure 8f) and as HFCA synthesis is not highly affected by particle size, this explains their constant activity upon reuse. Interestingly, the surface composition of Ag_5Au_5 and Ag_7Au_3 changed slightly (Figure 4a) but maintained their activity. For the silver-rich Ag_9Au_1 , a slight decrease in activity was observed after the third catalytic cycle, but the particle size was unaffected by recycling (Figure 8f, Figure S15). Thus, the decreasing activity of Ag_9Au_1 might be related to the deposition of impurities from HMF degradation,^[53] because the carbon balance was less than 100% and no drastic changes in the surface composition were found. Since monometallic Ag-based catalysts deactivate more rapidly under comparable reaction conditions,^[19] alloy formation with less than 90% of Ag greatly enhances the catalyst stability.

Ag_3Au_7 , which was tested at an elevated reaction temperature of 125°C for FDCA synthesis, decreased in activity after the first catalytic reaction, giving HFCA as the main product with a yield of 38% in the second reaction. For this catalyst, the particle size increased from 6.9 to 10.2 nm after the first catalytic reaction (Figure 8f, Figure S15) probably due to the higher reaction temperature applied for this catalyst. On the other hand, EDX scans and the surface composition derived by XPS did not show severe changes (Figures S6–S9, Figure S17). Although the particle size effect may be limited for Ag–Au alloys, this catalyst was the only one active in FDCA production, thus probably having active Au sites. Together with the high Au content and smaller particles favoring FDCA synthesis,^[51] sintering seems to be the primary reason for the deactivation of this catalyst.

In general, the reuse stability of catalysts active in HFCA synthesis was greatly enhanced by alloy formation of Ag and Au and the catalysts were also structurally stable.

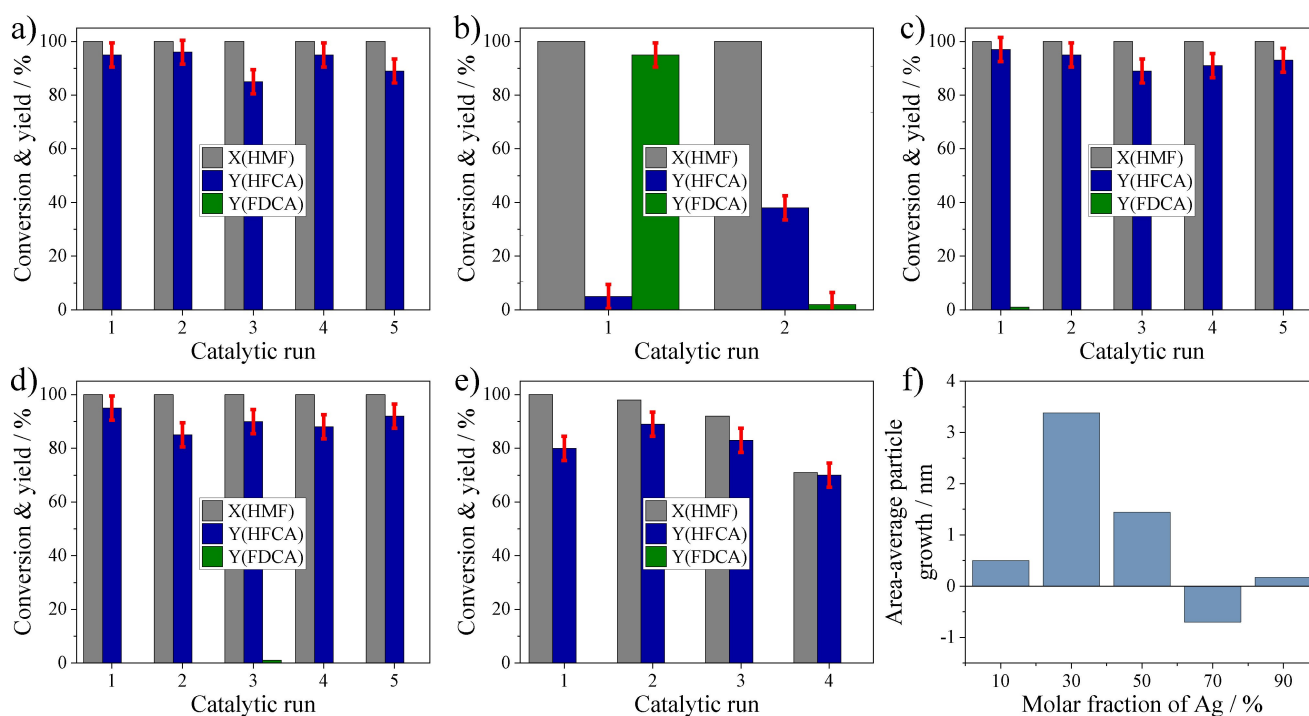


Figure 8. (a–e) Recycling experiments of the $\text{Ag}_x\text{Au}_{10-x}/\text{ZrO}_2$ catalysts and (f) changes in the mean particle size of each catalyst upon re-use. Reaction conditions: 1 mmol HMF in a total volume of 10 mL, HMF:M 100:1; (a) Ag_1Au_9 – room temperature, 10 bar air, HMF:NaOH 1:2; (b) Ag_3Au_7 – 125 °C, 10 bar air, HMF:NaOH 1:2; (c) Ag_5Au_5 – 75 °C, 10 bar air, HMF:NaOH 1:2; (d) Ag_7Au_3 – 75 °C, 10 bar air, HMF:NaOH 1:2; (e) Ag_9Au_1 – room temperature, 1 bar air, HMF:NaOH 1:1.

Mechanistic Outlook

In summary, differences in initial activity of the prepared catalysts were observed and can be mainly attributed to the particle composition due to similar particle sizes. The catalytic activities at room temperature and at 125 °C, i.e. HFCA and FDCA synthesis conditions, respectively, are summarized in Figure 9. An optimal composition for HMF oxidation activity can be concluded with Ag_3Au_7 being active both in aldehyde and alcohol oxidation, giving FDCA as the main product. The alcohol oxidation activity is lower for Ag_1Au_9 and Ag_5Au_5 and no activity in FDCA synthesis was observed at higher Ag content (Figure 9). Since the activation energy for aldehyde oxidation is lower,^[60] this step proceeds rapidly over all catalysts. The rate-limiting alcohol oxidation, on the other hand, has a higher energy barrier and only occurs on Au catalysts, as Ag is inactive in FDCA synthesis.^[19a] Besides activation barriers, oxygen activation is a crucial factor, which is limited on Au^[61] or limited to active Au sites possibly forming a perimeter with the support similar to literature on selective alcohol oxidation with Au/TiO_2 .^[62] Since hydroxide ions form a geminal diol in solution by nucleophilic attack on the aldehyde moiety of HMF, which is then dehydrogenated, oxygen is not incorporated in the oxidized molecule and thus has an indirect role in the

mechanism by removal of electrons and adsorbed H-species.^[60,63]

During oxygen activation, hydrogen peroxide is formed, whose decomposition has a high energy barrier on Au but proceeds readily on Ag or Ag–Au alloys.^[64] Consequently, two different kinds of active centers for HMF oxidation are present in Ag–Au catalysts (Figure 9c). The catalysts differed in bulk and surface composition (Table 1, Figure 4a). This alters the oxygen activation and respective selectivity to either only oxidize the aldehyde moiety or both functional groups of HMF with Ag active in oxygen activation and Au active in HMF conversion.^[21a]

While catalysts with higher amounts of either one of both metals favor alcohol oxidation (Figure 9a–c) an ideal catalyst for FDCA synthesis should have an optimal Ag:Au-ratio, which may result in a favorable amount of Ag atoms next to Au atoms. Based on in-depth characterization and extensive catalytic testing, Ag_3Au_7 was identified to have the most favorable Ag:Au ratio of 38:62 with active centers for alcohol oxidation *i.e.* FDCA synthesis.

All catalysts other than Ag_3Au_7 gave HFCA as the main product with enhanced stability. While pure Au and Ag catalysts deactivate by particle growth,^[19a] sintering was significantly reduced for the bimetallic catalysts except for Ag_3Au_7 .

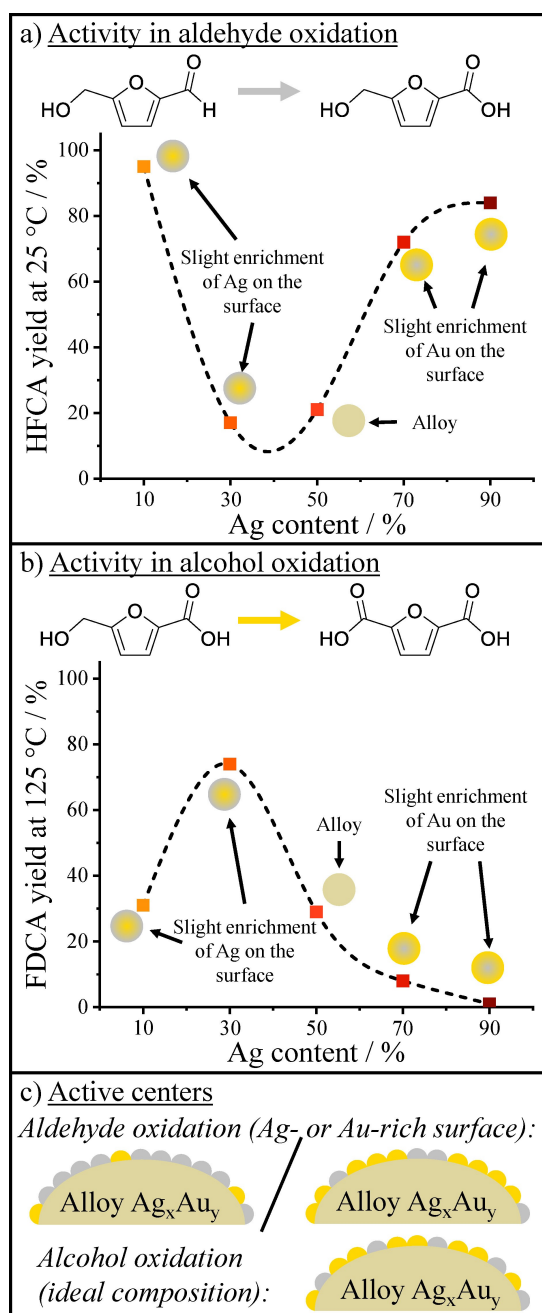


Figure 9. Schematic representation of the influence of the catalyst composition and structure on the activity in (a) aldehyde and (b) alcohol oxidation of HMF over Ag_xAu_{10-x}/ZrO_2 catalysts as well as (c) active centers. The respective product yields are taken from the temperature screening at 25 °C (active conditions for aldehyde oxidation) and 125 °C (active conditions for alcohol oxidation). Lines are added to guide the eye. Reaction conditions are shown in Figure 5.

Conclusion

The influence of alloy formation of Ag and Au on the catalytic activity in HMF oxidation was investigated. For this, we took a rational approach starting from the

synthesis of bimetallic nanoparticles with varying Ag/Au ratio followed by extensive catalytic studies. LAL allowed the production of highly pure bimetallic nanoparticles with comparable moderate particle sizes without any surfactant or organic ligand. Thus, catalytic oxidation activities can be linked directly to the catalyst composition. Particle sizes were maintained upon adsorption of colloids on ZrO_2 , as shown by TEM. The supported catalysts still contained alloyed nanoparticles with slight Ag-enrichment in the surface-near volume for high Au content and about 10% enrichment of Au in the surface-near volume at high Ag content as shown by a combination of XAS and XPS. Catalytic tests in HMF oxidation revealed differences in selectivity towards HFCA or FDCA depending on the composition. Optimization of the reaction conditions for each catalyst allowed the production of both HFCA and FDCA in yields above 90% and high productivity rates. At high Ag content, catalysts were active in HFCA synthesis, whereas the high Au content in Ag_3Au_7 and Ag_1Au_9 featured the FDCA synthesis, with an optimal activity for Ag_3Au_7 . Thus, a synergistic effect between Ag and Au was shown in varying selectivity and enhanced catalyst stability against sintering for most catalysts. The observed optimal compositions for either HFCA (Ag_9Au_1) or FDCA (Ag_3Au_7) formation might be linked to an ideal ratio of surface Ag and Au atoms, and respective oxygen activation to either promote selective aldehyde oxidation or both aldehyde and alcohol oxidation. For the future, it might be rewarding to substitute the homogeneous base by a solid base as catalyst support. All catalysts were stable against metal leaching under the reaction conditions applied in this study, and recycling experiments revealed great catalyst stability of Ag_1Au_9 , Ag_5Au_5 and Ag_7Au_3 , which also preserved their structure. Hence, the highly active and stable bimetallic Ag–Au catalysts may be suitable for future tests on the scale-up or the continuous oxidation of HMF.

Experimental Section

General Remarks

Sheets of pure Ag–Au alloys in five different compositions (Ag_xAu_{10-x} , $x = 1/3/5/7/9$, Research Institute for Precious Metals and Metal Chemistry, Schwäbisch Gmünd), HMF, FDCA, HFCA, NaOH, NaCl (Sigma-Aldrich/Merck), 5-formyl-2-furoic acid, 2,5-diformylfuran (TCI Chemicals), ZrO_2 1/8" pellets (Alfa Aesar) and synthetic air (Air Liquide) were used in analytical grade without further purification.

Catalyst preparation

In a first step, the alloy nanoparticles (AgAu NPs) were synthesized by laser ablation of an alloy target in flowing micromolar aqueous saline, followed by electrostatic adsorption

of the AgAu NPs in a dispersion of the ZrO₂ support material by adjusting the pH to 3.8 between the isoelectric points (IEP) of both reactants (Figure 2a).^[42,65]

In brief, the experimental laser ablation setup to synthesize the AgAu NPs consists of a flow chamber containing the alloy target, a piston pump (Ismatec ISM321 C) and a magnetically stirred beaker that was filled with an aqueous (Milli-Q water, resistivity 18.2 MΩ cm) 200 μM NaCl solution.^[34a] The respective alloy target foil (dimensions: 50 mm*20 mm*0.5 mm) was fixed inside the ablation chamber. The liquid layer in front of the target was set by the chamber window and fixed to 4 mm.^[34a] The piston pump was set to a flow rate of 50 mL min⁻¹ and the liquid was circulated through PTFE tubes. For the ablation, a nanosecond laser from Edgewave (model: IS160-1-T) operating with a pulse duration of 8 ns, a repetition rate of 5 kHz, a pulse energy of 8 mJ, and a wavelength of 532 nm was focused onto the target. The second harmonic laser wavelength was chosen to additionally reduce particle size by laser fragmentation of already produced colloids when passing through the ablation zone during cycling.^[34a] During ablation, the laser pulses were directed in a rectangular pattern using a scanner (Raylase SS-III-12) at a scan rate of 2000 mm s⁻¹ to minimize cavitation bubble shielding. The presence of the 200 μM NaCl solution allowed an *in situ* size quenching and to prevent agglomeration as well as particle growth.^[66] The ablation was conducted between 30 min (Ag₁Au₀) up to 120 min (Ag₉Au₁) depending on the target composition, as the ablation rate scales with the target density.^[67] The mass concentration of colloids was determined gravimetrically by differential weighting of the target with a microbalance (ABT 120-5DM from KERN) before and after LAL, as well as UV-Vis extinction spectroscopy of the colloids (Figure 2b).

For supporting the nanoparticles, 5 g of ZrO₂ was suspended in 200 ml of deionized water (Milli-Q water, resistivity 18.2 MΩ cm) in individual, continuously stirred batches. 0.1 g of AgAu NPs were added as colloids in respective volumes based on the measured concentrations after ablation to reach a mass loading of 2 wt.%. To improve the electrostatic adsorption of the AgAu NP to the ZrO₂ microparticles, the pH was adjusted to pH 3.8.^[42] After that, the suspension was allowed to sediment. The deposition efficiency was derived from the supernatant phase *via* UV-Vis extinction spectroscopy. The sedimented catalyst was separated by decantation and freeze-drying (Christ Alpha 1-4 LSCplus).

Catalyst Characterization

The catalysts were thoroughly characterized using multiple methods. Analytical disc centrifugation (ADC) was performed to determine AgAu NP sizes of the freshly prepared particles. UV-Vis and diffuse reflectance (DR) UV-Vis spectra were recorded to study alloy formation of the freshly prepared and the supported AgAu NPs, respectively. The particle size of supported AgAu NPs was determined by transmission electron microscopy (TEM). Inductively coupled plasma optical emission spectroscopy (ICP-OES) was used to verify metal loadings and molar compositions of the supported catalysts and N₂ physisorption using the Brunauer-Emmett-Teller method was employed to determine the specific surface area of the solid catalysts. Powder X-ray diffraction (XRD) patterns were

measured to study crystalline phases of supported catalysts. The surface composition and oxidation states of both metals were investigated using X-ray photoelectron spectroscopy (XPS). The degree of alloy formation and the local structure in the bulk AgAu NPs was investigated by X-ray absorption spectroscopy (XAS), which was recorded at the CAT-ACT beamline of the KIT synchrotron^[68] and *Athena* and *Artemis* software from the IFEFFIT/Demeter package (version 0.9.25)^[69] were used for data analysis.

For further details and experimental procedures, consult the Supporting Information of this article.

Catalytic Tests

Selective oxidation of HMF was carried out in Teflon[®] inlets (52 mL), which were placed in home-built magnetically stirred stainless steel autoclaves equipped with pressure inlet and outlet, manometer, thermocouple, and a relief valve. The reactors were charged with appropriate amounts of 0.2 M HMF solution, 2.5 M NaOH and distilled water to give a total volume of 10 mL in each reaction. The catalyst powders were added at a constant HMF-to-metal molar ratio (HMF:M; M = sum of metal content Ag and Au) based on the metal loading of each catalyst, and the reactors were sealed and purged three times with synthetic air before the desired pressure was adjusted. The reaction temperature was set in a controller and the autoclaves were heated with heating sleeves based on the thermocouple inside the reaction solution. The temperature was kept constant with a maximum variation of 1 °C and the starting point of each reaction was set after the solution first reached the set reaction temperature. Additional reactions were performed in a batch reactor with the same specifications that was equipped with a mechanical gas entrainment impeller. After the reactions, the reactors were quenched in an ice bath, depressurized, and the catalysts were separated by decantation.

Samples for analysis by high-performance liquid chromatography (HPLC) were taken before and after the catalytic tests, filtered with 0.45 μm Teflon filters and diluted according to the calibration range. HPLC was measured on a Hitachi Primaide at 50 °C and 25 °C (Bio-Rad Aminex HPX-87H column, solvent 5 mM H₂SO₄). The compounds were detected by a refractive index (Hitachi Chromaster 5450) and a diode array (Hitachi 1430) detector. Reference solutions of HMF, HFCA, FDCA, DFF and FFCA were used for calibration as external standards and concentrations of reaction solutions were derived from the peak areas. HMF conversion (eq 1), product yield (eq 2) and selectivity (eq 3), as well as the carbon balance (eq 4), were calculated based on the concentrations determined by HPLC.

$$X(\text{HMF}) = \frac{n(\text{HMF})_{\text{initial}} - n(\text{HMF})_{\text{final}}}{n(\text{HMF})_{\text{initial}}} \quad (1)$$

$$Y(x) = \frac{n(x)_{\text{final}}}{n(\text{HMF})_{\text{initial}}} \quad (2)$$

$$S(x) = \frac{n(x)_{\text{final}}}{n(\text{HMF})_{\text{initial}} - n(\text{HMF})_{\text{final}}} \quad (3)$$

$$C - \text{balance} = \frac{\sum n(x)_{\text{final}}}{n(\text{HMF})_{\text{initial}}} \quad (4)$$

Error bars were derived from Student's t-distribution with 95% confidence interval (two tailed t-test), a degree of freedom of 4 (5 recycling cycles) and the standard deviation of the respective recycling experiment. The standard deviation was calculated from samples shown in Figure 8c) as the sample showed good cycle stability. Consequently, as slight degradation might add to the error evaluation, error bars can be considered a worst-case estimation.

FDCA could be extracted by acidification of the reaction solutions with high FDCA yield to a pH value of 1 with HCl. For HFCA, the acidified solution was extracted with ethyl acetate and the solvent was removed under reduced pressure. The purity of both products was confirmed by ^1H and ^{13}C NMR spectroscopy, which was measured at room temperature in DMSO- d_6 on a Bruker Avance 250 and a Bruker Avance 400 spectrometer (Figure S21).

Acknowledgements

We acknowledge the KIT light source for provision of beamtime at the CAT-ACT beamline and the Institute of Beam Physics and Technology (IBPT) for the operation of the storage ring, the Karlsruhe Research Accelerator (KARA). We are grateful to Dr. Anna Zimina and Dr. Tim Prüßmann (IKFT/KIT) for providing assistance and technical support during the beamtime as well as Angela Deutsch (ITCP/KIT, N_2 physisorption), Armin Lautenbach (IKFT/KIT, ICP-OES) and Dr. Thomas Bergfeld (IAM-AMP/KIT, ICP-OES). Laser ablation and materials for Ag-Au alloy nanoparticles were funded by the Deutsche Forschungsgemeinschaft (DFG) (Project number: 356685838). Open access funding enabled and organized by Projekt DEAL.

References

- [1] a) D. Esposito, M. Antonietti, *Chem. Soc. Rev.* **2015**, *44*, 5821–5835; b) B. J. Nikolau, M. A. D. N. Perera, L. Brachova, B. Shanks, *Plant J.* **2008**, *54*, 536–545; c) Z. Zhang, G. W. Huber, *Chem. Soc. Rev.* **2018**, *47*, 1351–1390; d) E. Henrich, N. Dahmen, E. Dinjus, J. Sauer, *Chem. Ing. Tech.* **2015**, *87*, 1667–1685.
- [2] a) R.-J. van Putten, J. C. van der Waal, E. de Jong, C. B. Rasendra, H. J. Heeres, J. G. de Vries, *Chem. Rev.* **2013**, *113*, 1499–1597; b) D. M. Alonso, S. G. Wettstein, J. A. Dumesic, *Chem. Soc. Rev.* **2012**, *41*, 8075–8098.
- [3] A. A. Rosatella, S. P. Simeonov, R. F. M. Frade, C. A. M. Afonso, *Green Chem.* **2011**, *13*, 754–793.
- [4] M. Chatterjee, T. Ishizaka, H. Kawanami, *Green Chem.* **2014**, *16*, 4734–4739.
- [5] M. Chatterjee, T. Ishizaka, A. Chatterjee, H. Kawanami, *Green Chem.* **2017**, *19*, 1315–1326.
- [6] a) B. Saha, C. M. Bohn, M. M. Abu-Omar, *ChemSusChem* **2014**, *7*, 3095–3101; b) K. Hengst, M. Schubert, W. Kleist, J.-D. Grunwaldt, in: *Catalytic Hydrogenation for Biomass Valorization*, The Royal Society of Chemistry, Cambridge, UK, **2014**, pp. 125–150.
- [7] Z. Zhang, K. Deng, *ACS Catal.* **2015**, *5*, 6529–6544.
- [8] a) H. Hirai, *J. Macromol. Sci. A* **1984**, *21*, 1165–1179; b) M. Ventura, A. Dibenedetto, M. Aresta, *Inorg. Chim. Acta* **2018**, *470*, 11–21.
- [9] a) T. Werpy, G. Petersen, A. Aden, J. Bozell, J. Holladay, J. White, A. Manheim, US Department of Energy *Natural Renewable Energy Laboratory* **2004**; b) J. J. Bozell, G. R. Petersen, *Green Chem.* **2010**, *12*, 539–554.
- [10] a) M. Munekata, G. Tamura, *Agric. Biol. Chem.* **1981**, *45*, 2149–2150; b) A. C. Braisted, J. D. Oslob, W. L. Delano, J. Hyde, R. S. McDowell, N. Waal, C. Yu, M. R. Arkin, B. C. Raimundo, *J. Am. Chem. Soc.* **2003**, *125*, 3714–3715.
- [11] T. Miura, H. Kakinuma, T. Kawano, H. Matsuhisa (Canon Kabushiki Kaisha), *US Patent* 7,411,078, **2008**.
- [12] P. Anastas, N. Eghbali, *Chem. Soc. Rev.* **2010**, *39*, 301–312.
- [13] a) W. Partenheimer, Vladimir V. Grushin, *Adv. Synth. Catal.* **2001**, *343*, 102–111; b) C. M. d. Diego, W. P. Schammel, M. A. Dam, G. J. M. Gruter (Furanix Technologies B. V.), *US Patent* 8,519,167, **2013**.
- [14] Y. Hui, S. Zhang, W. Wang, *Adv. Synth. Catal.* **2019**, *361*, 2215–2235.
- [15] S. E. Davis, B. N. Zope, R. J. Davis, *Green Chem.* **2012**, *14*, 143–147.
- [16] E.-S. Kang, D. W. Chae, B. Kim, Y. G. Kim, *J. Ind. Eng. Chem.* **2012**, *18*, 174–177.
- [17] a) K. Mitsukura, Y. Sato, T. Yoshida, T. Nagasawa, *Biotechnol. Lett.* **2004**, *26*, 1643–1648; b) Y.-Z. Qin, Y.-M. Li, M.-H. Zong, H. Wu, N. Li, *Green Chem.* **2015**, *17*, 3718–3722.
- [18] a) Z. Zhang, B. Liu, K. Lv, J. Sun, K. Deng, *Green Chem.* **2014**, *16*, 2762–2770; b) F. Wang, Z. Zhang, *J. Inst. Chem.* **2017**, *70*, 1–6.
- [19] a) O. R. Schade, K. F. Kalz, D. Neukum, W. Kleist, J.-D. Grunwaldt, *Green Chem.* **2018**, *20*, 3530–3541; b) J. An, G. Sun, H. Xia, *ACS Sustainable Chem. Eng.* **2019**, *7*, 6696–6706.
- [20] a) A. Villa, M. Schiavoni, S. Campisi, G. M. Veith, L. Prati, *ChemSusChem* **2013**, *6*, 609–612; b) S. Albonetti, T. Pasini, A. Lolli, M. Blosi, M. Piccinini, N. Dimitratos, J. A. Lopez-Sanchez, D. J. Morgan, A. F. Carley, G. J. Hutchings, F. Cavani, *Catal. Today* **2012**, *195*, 120–126.
- [21] a) T. Benkó, A. Beck, K. Frey, D. F. Srankó, O. Geszti, G. Sáfrán, B. Maróti, Z. Schay, *Appl. Catal. A* **2014**, *479*, 103–111; b) X. Huang, X. Wang, X. Wang, X. Wang, M. Tan, W. Ding, X. Lu, *J. Catal.* **2013**, *301*, 217–226; c) R. Vadakkekara, M. Chakraborty, P. A. Parikh, *J. Inst. Chem.* **2015**, *50*, 84–92.
- [22] C.-W. Yen, M.-L. Lin, A. Wang, S.-A. Chen, J.-M. Chen, C.-Y. Mou, *J. Phys. Chem. C* **2009**, *113*, 17831–17839.
- [23] A. Wittstock, V. Zielasek, J. Biener, C. Friend, M. Bäumer, *Science* **2010**, *327*, 319–322.
- [24] A. Sandoval, A. Aguilar, C. Louis, A. Traverse, R. Zanella, *J. Catal.* **2011**, *281*, 40–49.

- [25] D. I. Kondarides, X. E. Verykios, *J. Catal.* **1996**, *158*, 363–377.
- [26] S. Hannemann, J.-D. Grunwaldt, F. Krumeich, P. Kappen, A. Baiker, *Appl. Surf. Sci.* **2006**, *252*, 7862–7873.
- [27] N. K. Chaki, H. Tsunoyama, Y. Negishi, H. Sakurai, T. Tsukuda, *J. Phys. Chem. C* **2007**, *111*, 4885–4888.
- [28] N. Blommaerts, H. Vanrompay, S. Nuti, S. Lenaerts, S. Bals, S. W. Verbruggen, *Small* **2019**, *15*, 1902791.
- [29] H. S. Oh, J. H. Yang, C. K. Costello, Y. M. Wang, S. R. Bare, H. H. Kung, M. C. Kung, *J. Catal.* **2002**, *210*, 375–386.
- [30] a) M. P. Mallin, C. J. Murphy, *Nano Lett.* **2002**, *2*, 1235–1237; b) J. Sanchez-Ramirez, U. Pal, L. Nolasco-Hernandez, J. Mendoza-Alvarez, J. Pescador-Rojas, *J. Nanomater.* **2008**, *2008*.
- [31] C. Rehbock, J. Jakobi, L. Gamrad, S. Van der Meer, D. Tiedemann, U. Taylor, W. Kues, D. Rath, S. Barcikowski, *Beilstein J. Nanotechnol.* **2014**, *5*, 1523–1541.
- [32] D. I. Sharapa, D. E. Doronkin, F. Studt, J. D. Grunwaldt, S. Behrens, *Adv. Mater.* **2019**, *31*, 1807381.
- [33] a) I. Lee, S. W. Han, K. Kim, *Chem. Commun.* **2001**, 1782–1783; b) S. Reichenberger, G. Marzun, M. Muhler, S. Barcikowski, *ChemCatChem* **2019**, *11*, 4489–4518; c) V. Amendola, D. Amans, Y. Ishikawa, N. Koshizaki, S. Scirè, G. Compagnini, S. Reichenberger, S. Barcikowski, *Chem. Eur. J.* **2020**, *26*, 9206–9242.
- [34] a) D. Zhang, B. Gökce, S. Barcikowski, *Chem. Rev.* **2017**, *117*, 3990–4103; b) A. Kanitz, M. Kalus, E. Gurevich, A. Ostendorf, S. Barcikowski, D. Amans, *Plasma Sources Science and Technology* **2019**, *28*, 103001.
- [35] a) C.-Y. Shih, R. Streubel, J. Heberle, A. Letzel, M. V. Shugaev, C. Wu, M. Schmidt, B. Gökce, S. Barcikowski, L. V. Zhigilei, *Nanoscale* **2018**, *10*, 6900–6910; b) S. Ibrahimkutti, P. Wagener, T. dos Santos Rolo, D. Karpov, A. Menzel, T. Baumbach, S. Barcikowski, A. Plech, *Sci. Rep.* **2015**, *5*, 16313; c) S. Barcikowski, A. Plech, K. S. Suslick, A. Vogel, *MRS Bull.* **2019**, *44*, 382–391.
- [36] a) A. Neumeister, J. Jakobi, C. Rehbock, J. Moysig, S. Barcikowski, *Phys. Chem. Chem. Phys.* **2014**, *16*, 23671–23678; b) A. Nastulyavichus, S. Kudryashov, N. Smirnov, A. Rudenko, A. Y. Kharin, N. Busleev, D. Zayarny, A. Ionin, D. Kirilenko, P. Brunkov, *Laser Phys. Lett.* **2019**, *16*, 096002.
- [37] a) S. Link, M. A. El-Sayed, *J. Phys. Chem. B* **1999**, *103*, 4212–4217; b) A. Henglein, *J. Phys. Chem.* **1993**, *97*, 5457–5471; c) A. Henglein, *Chem. Rev.* **1989**, *89*, 1861–1873.
- [38] S. Link, Z. L. Wang, M. El-Sayed, *J. Phys. Chem. B* **1999**, *103*, 3529–3533.
- [39] a) P. Mulvaney, *Langmuir* **1996**, *12*, 788–800; b) Y. Wang, Y. Ni, *Talanta* **2014**, *119*, 320–330.
- [40] Y.-H. Chen, C.-S. Yeh, *Chem. Commun.* **2001**, 371–372.
- [41] O. Prymak, J. Jakobi, C. Rehbock, M. Eppe, S. Barcikowski, *Mater. Chem. Phys.* **2018**, *207*, 442–450.
- [42] G. Marzun, C. Streich, S. Jendrzey, S. Barcikowski, P. Wagener, *Langmuir* **2014**, *30*, 11928–11936.
- [43] G. Marzun, J. Nakamura, X. Zhang, S. Barcikowski, P. Wagener, *Appl. Surf. Sci.* **2015**, *348*, 75–84.
- [44] a) S. Nishimura, A. T. N. Dao, D. Mott, K. Ebitani, S. Maenosono, *J. Phys. Chem. C* **2012**, *116*, 4511–4516; b) A. E. Russell, A. Rose, *Chem. Rev.* **2004**, *104*, 4613–4636.
- [45] C. Tyson, A. Bzowski, P. Kristof, M. Kuhn, R. Sammynaiken, T. Sham, *Phys. Rev. B* **1992**, *45*, 8924.
- [46] M. Kuhn, T. Sham, *Phys. Rev. B* **1994**, *49*, 1647.
- [47] T. Shibata, B. A. Bunker, Z. Zhang, D. Meisel, C. F. Vardeman, J. D. Gezelter, *J. Am. Chem. Soc.* **2002**, *124*, 11989–11996.
- [48] a) F. Liu, D. Wechsler, P. Zhang, *Chem. Phys. Lett.* **2008**, *461*, 254–259; b) G. Tofighi, A. Gaur, D. E. Doronkin, H. Lichtenberg, W. Wang, D. Wang, G. Rinke, A. Ewinger, R. Dittmeyer, J.-D. Grunwaldt, *J. Phys. Chem. C* **2018**, *122*, 1721–1731.
- [49] L. M. Moreau, C. A. Schurman, S. Kewalramani, M. M. Shahjamali, C. A. Mirkin, M. J. Bedzyk, *J. Am. Chem. Soc.* **2017**, *139*, 12291–12298.
- [50] L. Russo, V. Puentes, A. Merkoçi, *Nano Res.* **2018**, *11*, 6336–6345.
- [51] C. Megias-Sayago, A. Lolli, D. Bonincontro, A. Penkova, S. Albonetti, F. Cavani, J. A. Odriozola, S. Ivanova, *ChemCatChem* **2019**, *12*, 1177–1183.
- [52] K. R. Vuyyuru, P. Strasser, *Catal. Today* **2012**, *195*, 144–154.
- [53] O. Casanova, S. Iborra, A. Corma, *ChemSusChem* **2009**, *2*, 1138–1144.
- [54] O. Schade, P. Dolcet, A. Nefedov, X. Huang, E. Saraçi, C. Wöll, J.-D. Grunwaldt, *Catalysts* **2020**, *10*, 342–354.
- [55] A.-Q. Wang, C.-M. Chang, C.-Y. Mou, *J. Phys. Chem. B* **2005**, *109*, 18860–18867.
- [56] O. Schade, A. Gaur, A. Zimina, E. Saraçi, J.-D. Grunwaldt, *Catal. Sci. Technol.* **2020**, *10*, 5036–5047.
- [57] a) N. K. Gupta, S. Nishimura, A. Takagaki, K. Ebitani, *Green Chem.* **2011**, *13*, 824–827; b) Y. Wang, K. Yu, D. Lei, W. Si, Y. Feng, L.-L. Lou, S. Liu, *ACS Sustainable Chem. Eng.* **2016**, *4*, 4752–4761; c) X. Han, L. Geng, Y. Guo, R. Jia, X. Liu, Y. Zhang, Y. Wang, *Green Chem.* **2016**, *18*, 1597–1604.
- [58] a) Z. Gui, W. Cao, S. Saravanamurugan, A. Riisager, L. Chen, Z. Qi, *ChemCatChem* **2016**, *8*, 3636–3643; b) P. Zhang, X. Zhang, X. Kang, H. Liu, C. Chen, C. Xie, B. Han, *Chem. Commun.* **2018**, *54*, 12065–12068; c) Q. Wang, W. Hou, S. Li, J. Xie, J. Li, Y. Zhou, J. Wang, *Green Chem.* **2017**, *19*, 3820–3830; d) X. Wan, C. Zhou, J. Chen, W. Deng, Q. Zhang, Y. Yang, Y. Wang, *ACS Catal.* **2014**, *4*, 2175–2185.
- [59] T. Pasini, M. Piccinini, M. Blosi, R. Bonelli, S. Albonetti, N. Dimitratos, J. A. Lopez-Sanchez, M. Sankar, Q. He, C. J. Kiely, G. J. Hutchings, F. Cavani, *Green Chem.* **2011**, *13*, 2091–2099.
- [60] B. N. Zope, D. D. Hibbitts, M. Neurock, R. J. Davis, *Science* **2010**, *330*, 74–78.
- [61] V. Sobyanin, V. Gorodetskii, N. Bulgakov, *React. Kinet. Catal. Lett.* **1977**, *7*, 285–290.

- [62] M. Farnesi Camellone, J. Zhao, L. Jin, Y. Wang, M. Muhler, D. Marx, *Angew. Chem.* **2013**, *125*, 5892–5896; *Angew. Chem. Int. Ed.* **2013**, *52*, 5780–5784.
- [63] S. E. Davis, M. S. Ide, R. J. Davis, *Green Chem.* **2013**, *15*, 17–45.
- [64] K. Goszner, H. Bischof, *J. Catal.* **1974**, *32*, 175–182.
- [65] a) J. Moon, H. Lee, J. Kim, G. Kim, D. Lee, H. Lee, *Mater. Lett.* **1999**, *38*, 214–220; b) M. Schultz, W. Burckhardt, *Solid State Ionics* **1993**, *63*, 18–24.
- [66] C. Rehbock, V. Merk, L. Gamrad, R. Streubel, S. Barcikowski, *Phys. Chem. Chem. Phys.* **2013**, *15*, 3057–3067.
- [67] S. Kohsakowski, F. Seiser, J.-P. Wiederrecht, S. Reichenberger, T. Vinnay, S. Barcikowski, G. Marzun, *Nanotechnology* **2019**, *31*, 095603.
- [68] A. Zimina, K. Dardenne, M. Denecke, D. Doronkin, E. Huttel, H. Lichtenberg, S. Mangold, T. Pruessmann, J. Rothe, T. Spangenberg, R. Steininger, T. Vitova, H. Geckeis, J. D. Grunwaldt, *Rev. Sci. Instrum.* **2017**, *88*, 113113.
- [69] B. Ravel, M. Newville, *J. Synchrotron Radiat.* **2005**, *12*, 537–541.